Cite this: *J. Mater. Chem. A*, 2018, 6, 21605

Insight into the intercalation mechanism of WSe₂ onions toward metal ion capacitors: sodium rivals lithium†

Yichun Wang,^{‡,ab} Xin Zhang,^{‡,ab} Peixun Xiong,^c Fuxing Yin,^{ab} Yunhua Xu,^{ID c} Biao Wan,^{de} Qingzhou Wang,^{ab} Gongkai Wang,^{ID *ab} Puguang Ji^{*ab} and Huiyang Gou^{*e}**HPSTAR**
659-2018

WSe₂ onions were synthesized using a homemade chemical vapor deposition (CVD) method. The formation of a very fine particle size and spherical microstructure was attributed to the fast cooling rate and reduction of the surface energy of two-dimensional (2D) WSe₂ after nucleation and growth during the synthesis process. A specific capacity of 205 mA h g⁻¹ at 10 A g⁻¹ vs. sodium ions can be reached, representing the best sodium ion rate capability ever reported for WSe₂. An exceptionally high capacitive contribution showed that fast intercalation kinetics were present, which were attributed to the intrinsic properties and the unique microstructure of WSe₂. Sodium ions could be stored faster than lithium ions throughout WSe₂ due to the different intercalation mechanisms, as concluded from electrochemical investigations and simulation. The sodium ion capacitors (SICs) delivered superior energy/power densities (the maximum energy density is 123.1 W h kg⁻¹ and the maximum power density is 14.1 kW kg⁻¹), demonstrating that WSe₂ is a promising alternative for SICs that could rival lithium ion capacitors (LICs) and shedding new light on novel 2D material design of SICs with high energy/power densities.

Received 25th September 2018
Accepted 16th October 2018

DOI: 10.1039/c8ta09286a

rsc.li/materials-a

1. Introduction

Massive improvements in the performance of electrochemical energy storage (EES) devices have stimulated research interest into electrochemical capacitors, which are important in a range of applications, from consumer electronics to national grids.^{1,2} Understanding the operating mechanism of electrochemical capacitors is key to the development of qualified electrode materials.^{3,4} Electrochemical capacitors, or electrical double-layer capacitors (EDLCs), deliver extremely high power densities through reversible ion adsorption at the interface between

the electrode and electrolyte, while suffering from a limited charge capacity. To improve the energy density while maintaining a high power output, an alternative energy-storage mechanism for battery-supercapacitor hybrid devices, namely metal ion capacitors (MICs), has been developed and widely investigated.⁵⁻⁷ Lithium ion capacitors (LICs) have attracted great attention owing to the compelling energy/power densities they can produce in one cell and their long service life. Normally, LICs consist of a battery-type anode and EDLC-type cathode that are operated through combined mechanisms of lithium ion intercalation/deintercalation at the anode and anion double-layer adsorption/desorption at the cathode.^{8,9} However, the performance of the battery-type anode is usually limited by solid-state diffusion, resulting in a kinetic mismatch with respect to the cathode. This kinetic barrier influences the charging/discharging time (power density) of LICs, eventually resulting in inferior batteries.¹⁰⁻¹³ Therefore, anode materials that afford high rate capabilities will boost the development of high-performance LICs.

Various strategies have been used to develop superior anode materials with respectable rate behaviors, including nanoscale tailoring of the microstructure, doping, and integrating with carbonaceous additives.¹⁴⁻¹⁸ Indeed, much progress has been made using these techniques, denoted as the external factor. However, the intrinsic properties of the materials, denoted as the internal factor, should not be neglected. A well-known intrinsic property is pseudocapacitance, which mainly relies

^aSchool of Material Science and Engineering, Research Institute for Energy Equipment Materials, Hebei University of Technology, Tianjin, 300130, China. E-mail: wang.gongkai@hebut.edu.cn; jipuguang@hebut.edu.cn

^bTianjin Key Laboratory of Materials Laminating Fabrication and Interface Control Technology, Tianjin 300130, China

^cSchool of Materials Science and Engineering, Key Laboratory of Advanced Ceramics and Machining Technology (Ministry of Education), Tianjin Key Laboratory of Composite and Functional Materials, Tianjin Key Laboratory of Molecular Optoelectronic Science, Tianjin University, Tianjin 300072, China

^dKey Laboratory of Metastable Materials Science and Technology, College of Material Science and Engineering, Yanshan University, Qinhuangdao 066004, China

^eCenter for High Pressure Science and Technology Advanced Research, Beijing 100094, China. E-mail: huiyang.gou@hpstar.ac.cn

† Electronic supplementary information (ESI) available. See DOI: 10.1039/c8ta09286a

‡ These authors contributed equally to this work.

on charge transfer at or near the redox active material surface (such as $\text{RuO}_2 \cdot \text{H}_2\text{O}$, MnO_2 , and Nb_2O_5) or ion intercalation without phase transformation. As the charge transfer and storage process is independent of electrode solid-state diffusion, pseudocapacitive materials usually deliver high rate capabilities.^{19,20} Dunn *et al.* reported using mesoporous MoS_2 as an anode material for lithium ions, which afforded a specific capacity of 140 mA h g^{-1} in a charging/discharging time of 20 s and showed a superior cycle life at this lithium capacity. A detailed electrochemical analysis clarified the pseudocapacitive energy storage mechanism, making MoS_2 a promising anode for EES.²¹

Inspired by this, many battery-type materials, usually exhibiting clearly separated redox peaks in cyclic voltammograms, have been evaluated to explore their analogous properties.^{22–24} For example, Xiong *et al.* reported graphene-coated TiO_2 nanoparticles as anodes for sodium storage that could deliver a specific capacity of up to 101 mA h g^{-1} at a current rate of 60C in which a surface-induced capacitive process provided an important contribution.²⁵ Shen *et al.* reported a new type of TiNb_2O_7 @carbon electrode for LICs that showed a superior rate performance that was also affected by the capacitive process.²⁶ This capacitive influence on the charge storage mechanism indicated a fast kinetics, leading to facial ion insertion/extraction and an exceptional rate capability. Undoubtedly, this feature is beneficial for MICs.

Using transition metal dichalcogenides (TMDs), such as MoS_2 , as two-dimensional (2D) materials has received significant attention. Compared with graphene, TMDs (formula: MX_2 , where M is a transition metal element, such as Mo, W, Ti, Pt, or Hf, and X is a chalcogen, such as S, Se, or Te) with striking physical and chemical properties exhibit versatile applications, particularly in EES.^{27,28} TMDs possess 2D layered structures with weak van der Waals interactions and rich electronic properties, which are generally beneficial for lithium ion diffusion and transport. Meanwhile, the flexible 2D structure could alleviate the strain derived from volume changes during the lithiation/delithiation process.²⁹ Similar to MoS_2 , tungsten diselenide (WSe_2) has a 2D layered structure that can achieve an interlayer spacing of 6.50 \AA , which is larger than that of graphite (3.35 \AA), and a theoretical capacity of 314 mA h g^{-1} and density of 9.32 g cm^{-3} . Although few reports on WSe_2 have been published, it is clearly a potential candidate for lithium ion storage.^{30–34} However, the intercalation mechanism of WSe_2 and its capacitive effect for capacitive storage remains mostly unexplored.

In addition to LICs, sodium ion capacitors (SICs) have drawn considerable interest because sodium is the most appealing alternative to lithium. Other than the larger ionic radius and atomic mass of sodium, sodium ion chemistry could benefit from the developed lithium ion system.^{35–38} The development of SICs with power/energy comparable to LICs through the rational design of electrodes and other components will maintain the sustainable development of electrical energy and decrease the economic and geopolitical impact. Herein, we have scrutinized WSe_2 as an anode for SICs and evaluated the intercalation mechanism with sodium ion chemistry.

In this work, WSe_2 onions were synthesized using a home-made chemical vapor deposition (CVD) method. A unique

onion-like morphology with an average particle size of 70 nm that provided sufficient active sites and short diffusion path for ions was obtained. Specific capacities of 211 and 205 mA h g^{-1} at 1.6 and 10 A g^{-1} were reached, corresponding to lithium and sodium ions, respectively. More importantly, a very high capacitive contribution ratio was obtained, indicating fast intercalation kinetics for both lithium and sodium ion reactions. Furthermore, sodium ions could be stored faster throughout WSe_2 than lithium ions, which was attributed to their different intercalation mechanisms. Detailed electrochemical investigations and simulations were performed. Both LICs and SICs were assembled using WSe_2 onions as the anode and activated carbon (AC) as the cathode, with SICs delivering energy/power densities comparable to LICs. This demonstrated WSe_2 as a promising alternative for SICs that could rival LICs.

2. Results and discussion

WSe_2 onions were synthesized through a CVD process in which $\text{W}(\text{CO})_6$ and pure selenium were used as W and Se precursors, respectively. Schematic illustrations are shown in Fig. 1a and S1 (ESI[†]), and experimental details are provided in the Experimental section. Selenium was always used in excess to obtain a mixture of WSe_2 and Se without W that was difficult to remove post-synthesis. As shown in Fig. 1b, in addition to the diffraction pattern of WSe_2 , obvious diffraction peaks corresponding to Se were observed (JCPDS no. 73-0465). After subsequent heat-treatment under H_2 , Se was fully eliminated, leaving pure phase WSe_2 (JCPDS no. 38-1388).³⁹ Raman spectroscopy was used to identify the purity of the as-synthesized WSe_2 . As shown in Fig. 1c, dominant characteristic peaks at around 249 cm^{-1} were assigned to the E_{2g}^1 (in-plane) mode, while the A_{1g} (out-of-plane) mode peak was not obvious due to the small energy difference between A_{1g} and E_{2g}^1 , which was consistent with previous reports.^{40,41}

The valence state and surface elemental composition of as-synthesized WSe_2 were determined by X-ray photoelectron spectroscopy (XPS), with the large survey spectrum shown in Fig. S2 (ESI[†]). Corresponding high resolution spectra of W 4f and Se 3d are shown in Fig. 1d. Characteristic peaks located at 54.9 and 54.1 eV with a spin-energy separation of 0.8 eV corresponded to Se $3d_{3/2}$ and Se $3d_{5/2}$, respectively. The W 4f spectrum showed two main peaks centered at 34 and 31.9 eV with a spin-energy separation of 2.1 eV, corresponding to W $4f_{5/2}$ and W $4f_{7/2}$, respectively. Accordingly, the valence states of W(IV) and Se(II) were confirmed, demonstrating that pure phase WSe_2 had been obtained.^{42,43}

The morphology and microstructure of the WSe_2 nanoparticles were observed by scanning electron microscopy (SEM) and transmission electron microscopy (TEM). As shown in Fig. 1e and f, spherical WSe_2 nanoparticles with an average size of around 70 nm and uniform distribution were observed. Considering the synthetic process (Fig. S1, ESI[†]), active W and Se precursors preferred to aggregate in the cooled chamber, which restricted the grain growth of WSe_2 due to the fast cooling rate, resulting in a fine particle size. TEM images gave insight into the inner structure. As shown in Fig. 1h–j, WSe_2 showed an

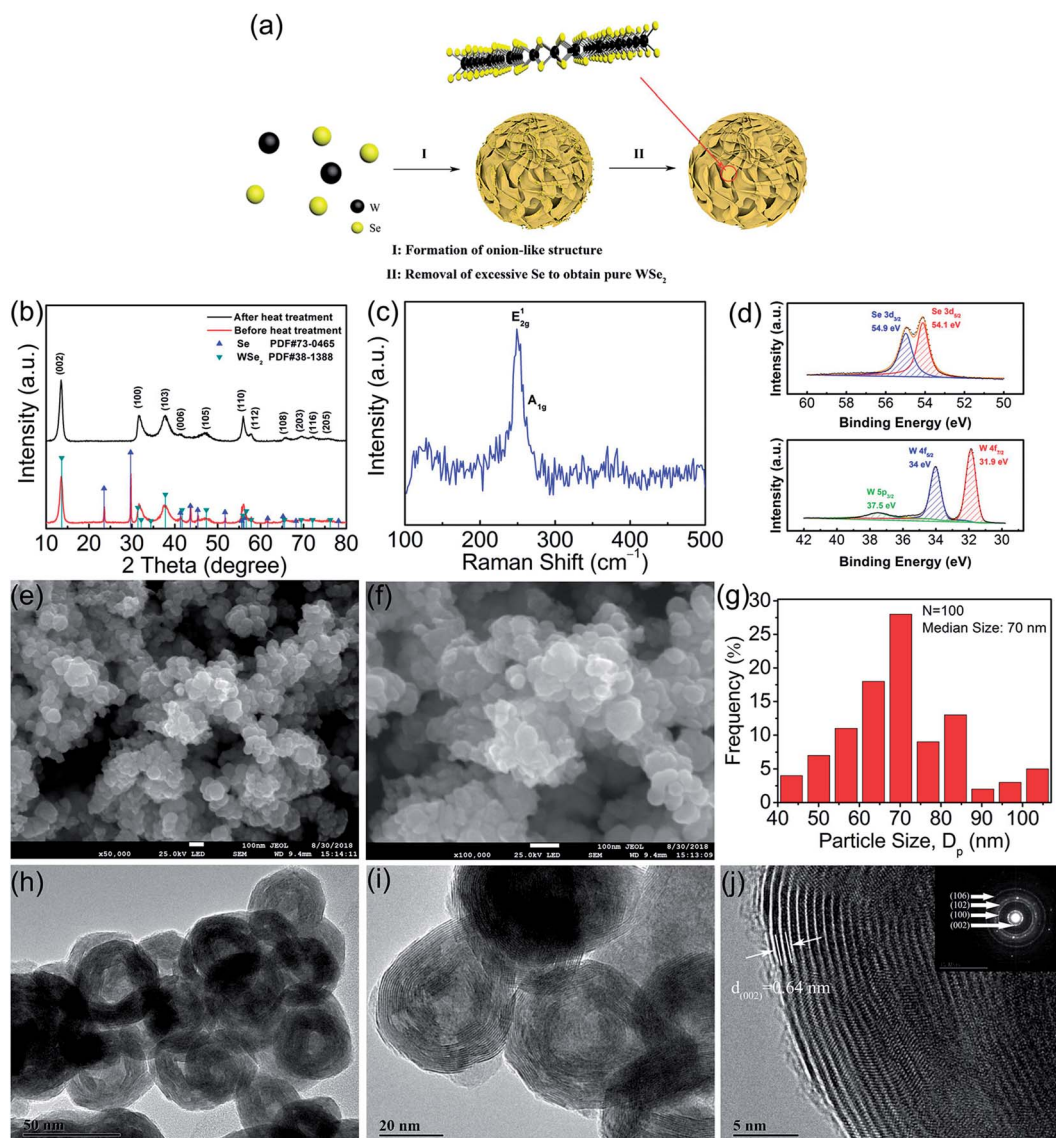


Fig. 1 (a) Schematic formation of WSe₂ nanoparticles. Characterization of the as-prepared WSe₂ nanoparticles: (b) XRD patterns, (c) Raman spectrum, and (d) XPS spectra of Se 3d, W 5p, and W 4f. Morphology and structure of the as-prepared WSe₂ nanoparticles: (e and f) SEM images, (g) corresponding particle size distribution, (h and i) TEM images, and (j) high-resolution TEM image and (inset) SAED pattern.

onion-like structure with abundant edges, in which the layered structure was clearly observed. Spherical structure formation might be due to the reduction of surface energy in 2D WSe₂ after nucleation and growth. A lattice fringe with interplanar spacing of 0.64 nm corresponded to the (002) plane of the hexagonal WSe₂ phase, which was consistent with the XRD results. The selected area electron diffraction (SAED) pattern was obtained, as shown in the inset of Fig. 1j. The WSe₂ phase with polycrystalline structure caused a group of diffraction rings correlating to the (002), (100), (102), and (106) planes of the WSe₂ phase, respectively, confirming the pure phase and unique structure of WSe₂ obtained under our experimental conditions.

Together with morphological analysis, the electrochemical behavior of WSe₂ using lithium and sodium ion chemistry was evaluated. Fig. 2a shows the representative cyclic voltammogram (CV) curves of WSe₂ in the lithium ion half-cell during the

initial four cycles at a scan rate of 0.1 mV s⁻¹ in the potential range 0.01–3.0 V (vs. Li⁺/Li). The first cycle was distinctly different from subsequent cycles. The strong peak at around 0.79 V (vs. Li⁺/Li) in the first cycle might be due to structure rearrangement and formation of the solid-electrolyte interphase (SEI) layer. In the following three cycles, another two cathodic peaks at 1.97 and 1.86 V (vs. Li⁺/Li) were obtained instead of the original peak, which was attributed to the intercalation of lithium ion into WSe₂ and eventual formation of Li_xWSe₂. The anodic peak was observed at around 2.28 V (vs. Li⁺/Li), which was ascribed to lithium ion extraction and reversible conversion back to WSe₂.^{31,32} Meanwhile, CV curves for the 2nd cycle showed a negligible change, indicating good electrochemical reversibility. Fig. 2b shows the corresponding galvanostatic charge/discharge profiles of the 1st, 2nd, 10th, 30th, and 50th cycles at a current density of 100 mA g⁻¹. A flat plateau at

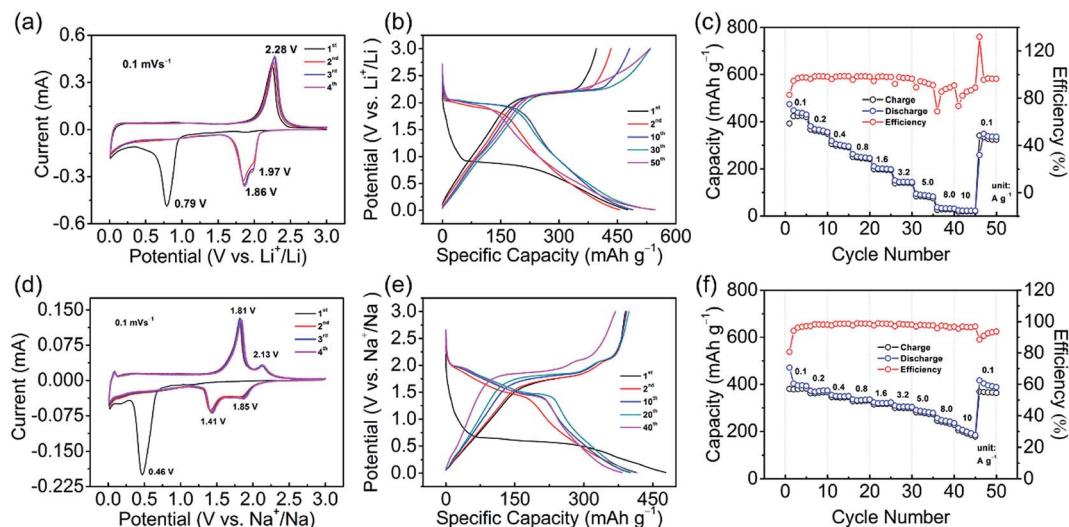


Fig. 2 Electrochemical characterization of WSe₂ vs. lithium and sodium. CV curves vs. (a) lithium and (d) sodium at a scan rate of 0.1 mV s⁻¹; galvanostatic charge/discharge profiles vs. (b) lithium and (e) sodium at a current density of 100 mA g⁻¹; and rate performance vs. (c) lithium and (f) sodium.

around 2.0 V with two sloping voltage curves was observed from the 2nd cycle onward, while a flat plateau was observed at around 1.0 V in the 1st cycle. Specific capacities of 476.4 and 546.3 mA h g⁻¹ were delivered in the 1st and 50th cycles, respectively, exhibiting good reversibility. The initial coulombic efficiency was about 83%, but as the cycle number increased, the coulombic efficiency was nearly 100% (Fig. S3a, ESI[†]). The corresponding electrochemical impedance spectroscopy (EIS) profiles (1st, 2nd, 10th, 30th, and 50th cycles) are shown in Fig. S3b (ESI[†]). All Nyquist plots consisted of a semicircle and an oblique line, corresponding to charge transfer resistance (R_{ct}) and lithium ion diffusion into the electrode.⁴⁴ The decreased R_{ct} indicated efficient charge transfer at the interface between the electrode and electrolyte, which might be attributed to refinement of the WSe₂ crystalline structure shortening the lithium ion diffusion path after the lithiation/delithiation process. WSe₂ delivered a specific capacity of 439 mA h g⁻¹ at a current density of 100 mA g⁻¹, while, the specific capacity remained at 250 mA h g⁻¹ at a current density of 800 mA g⁻¹. When the current rate reached 3.2 A g⁻¹, a specific capacity of 140 mA h g⁻¹ was obtained, indicating a good rate capability with respect to lithium ions. Meanwhile, a specific capacity of 350 mA h g⁻¹ was achieved as the current density was reset back to 100 mA g⁻¹, demonstrating a good electrochemical reversibility (Fig. 2c).

For sodium ion chemistry, the same evaluation was performed in the sodium ion half-cell. CV curves of WSe₂ during the initial four cycles at a scan rate of 0.1 mV s⁻¹ in the potential range 0.01–3.0 V (vs. Na⁺/Na) are shown in Fig. 2d. In contrast to the lithiation/delithiation process, the cathodic (1.41 V and 1.85 V) and anodic (1.81 V and 2.13 V) peak positions changed dramatically after the 1st sodiation/desodiation process. Meanwhile, two sets of cathodic and anodic peaks were observed, indicating the multistep electrochemical reaction of WSe₂ with sodium ions and different mechanism of sodiation/desodiation compared with that of lithiation/delithiation (respective

mechanisms will be discussed later). Fig. 2e shows the typical galvanostatic charge/discharge profiles of the 1st, 2nd, 10th, 30th, and 40th cycles at a current density of 100 mA g⁻¹. A relatively flat plateau at around 0.5 V was observed in the 1st cycle. Subsequently, an oblique curve in the range 1.3–2.1 V, corresponding to the potential plateau, was obtained from the 2nd cycle onward. Specific capacities of 478.1 and 383.0 mA h g⁻¹ were obtained in the 1st and 40th cycles, respectively, exhibiting a good reversibility. The initial coulombic efficiency was about 81.9% and reached nearly 100% as the cycle number increased (Fig. S3c, ESI[†]). EIS plots indicated the decreased R_{ct} after cycles, demonstrating microstructure rearrangement in the sodiation/desodiation process, analogous to that in the reaction with lithium ions (Fig. S3d, ESI[†]). Interestingly, WSe₂ exhibited an even better rate capability and reversibility in the sodium ion half-cell compared with the lithium ion half-cell. Specific capacities of 403 and 330 mA h g⁻¹ were obtained at current densities of 100 and 800 mA g⁻¹, respectively (Fig. 2f). When the current rate reached 10 A g⁻¹, the specific capacity was still 214 mA h g⁻¹, and when the current rate was reset back to 100 mA g⁻¹, a comparable specific capacity of 404 mA h g⁻¹ was obtained. Taking into account the larger ionic radius and atomic mass of sodium, using WSe₂ as the anode in sodium ion half-cells could achieve even better performance than a lithium ion anode. The remarkable rate performances for sodium ions were the best reported to date, as shown in Table S1.† In contrast, commercial WSe₂ was also applied as the anode under lithium ion and sodium ion conditions. The SEM images and rate performance are shown in Fig. S4,† exhibiting an inferior performance. The unique microstructures that provided abundant insertion channels and short diffusion length resulted in the WSe₂ anodes presenting superior rate behavior. The results for the WSe₂ anodes demonstrated the importance and advantages of our homemade CVD method, which offers a novel model for the synthesis of other 2D materials.

The electrochemical kinetics of WSe_2 with respect to lithium and sodium ion chemistry were examined using CV measurements. CV curves at various scan rates from 0.1 to 2.5 mV s^{-1} are shown in Fig. 3a and b, corresponding to lithium and sodium, respectively. Insets show the CV curves obtained at faster scan rates. All CV curves exhibited negligible distortion, demonstrating a superior voltammetric response. Notably, WSe_2 vs. sodium ions afforded a fast scan rate of up to 100 mV s^{-1} with small potential separation and a distinct current peak (Fig. 3b inset). Meanwhile, WSe_2 vs. lithium ions exhibited a relatively closed CV curve at a scan rate of up to 25 mV s^{-1} (Fig. 3a inset), indicating the smaller ohmic and/or diffusion constraints of WSe_2 vs. sodium ions at a high scan rate and with superior ion transport efficiency. The derived $\log(v) - \log(i)$ data obeys a power law relationship:

$$i = av^b \quad (1)$$

where i is the peak current and v is the scan rate. Typically, $b = 0.5$ represents a diffusion-controlled intercalation process, while $b = 1.0$ suggests a surface capacitive process.²⁰ With respect to lithium ions, WSe_2 exhibited b values of between 0.68 and 0.73, implying a diffusion-controlled mechanism accompanied by a surface-induced capacitive process (Fig. 3c). For sodium ions, b values of between 0.80 and 0.86 were obtained, demonstrating the intercalation reaction was significantly affected by the surface capacitive process and the superior rate behavior (Fig. 3d).

Considering that both energy storage mechanisms are coupled with various degrees of the capacitive process, the capacitive contribution should be determined to give insight

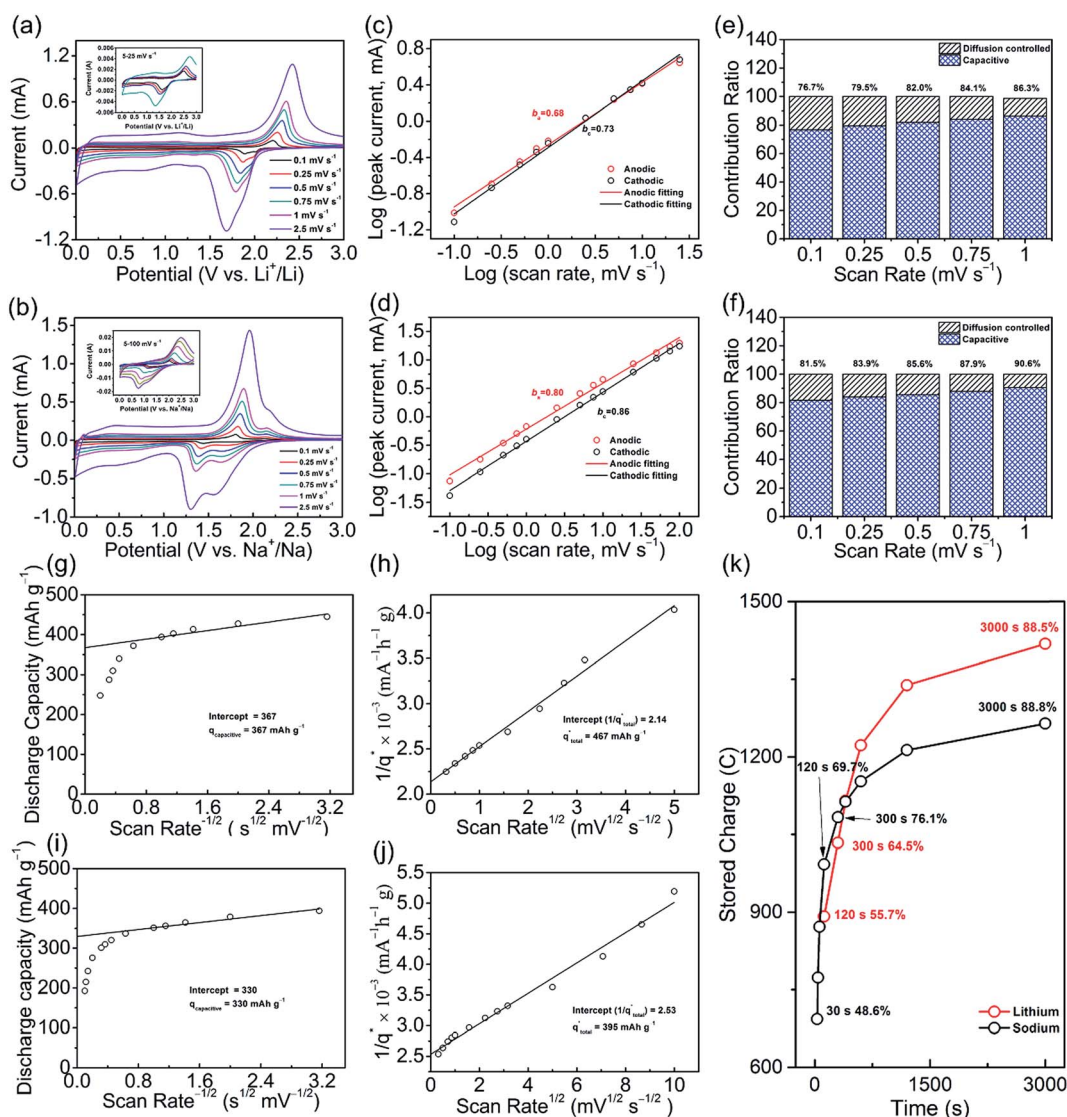


Fig. 3 Electrochemical kinetics analysis: CV curves at various scan rates vs. (a) lithium and (b) sodium; dependence of $\log(\text{scan rate})$ on $\log(\text{peak current})$ vs. (c) lithium and (d) sodium; contribution ratio of capacity at various scan rates vs. (e) lithium and (f) sodium; Trasatti analysis vs. lithium: (g) dependence of capacitive discharge capacity ($q(v)$) on scan rate $^{-1/2}$, (h) dependence of $1/q(v)$ on scan rate $^{1/2}$; Trasatti analysis vs. sodium: (i) dependence of capacitive discharge capacity ($q(v)$) on scan rate $^{-1/2}$, (j) dependence of $1/q(v)$ on scan rate $^{1/2}$; and (k) stored charge as a function of time vs. lithium and sodium.

into the electrochemical kinetics *vs.* lithium and sodium. Two methods were employed in this study, with the first making use of the relation between the response current at a fixed potential and scan rates according to the equation:

$$i(V) = k_1v + k_2v^{1/2} \quad (2)$$

where k_1 and k_2 can be determined using CV currents at different scan rates.^{25,45,46} Fig. 3e and f show the capacitive contributions at various scan rates from 0.1 to 1 mV s⁻¹, corresponding to lithium and sodium, respectively. WSe₂ *vs.* sodium ions exhibited a higher capacitive contribution at every scan rate compared with WSe₂ *vs.* lithium ions, with capacitive contributions of 81.5% and 90.6% at scan rates of 0.1 and 1 mV s⁻¹ *vs.* sodium ions compared with 76.7% and 86.3% *vs.* lithium ions. Meanwhile, the capacitive contribution gradually increased with increasing scan rate, indicating that the surface capacitive process dominated the electrochemical reaction. Fig. S5a and b (ESI[†]) show the potential regions where capacitive contributions occur in the CV curves at 1 mV s⁻¹ *vs.* lithium and sodium ions. These results indicated that the kinetics were strongly influenced by the capacitive process throughout potential range. More importantly, even higher capacitive contribution occurred in WSe₂ *vs.* sodium ions, which was consistent with the results shown in Fig. 3a and b.

The second method was Trasatti analysis, which defines the diffusion-controlled and capacitive charge storage processes according to the equations:

$$q(v) = q_{\text{capacitive}} + \alpha(v^{-1/2}) \quad (3)$$

$$\frac{1}{q(v)} = \frac{1}{q_{\text{total}}} + \alpha(v^{1/2}) \quad (4)$$

where $q(v)$ is the total voltammetric charge obtained from CV curves, $q_{\text{capacitive}}$ is the capacitive charge, q_{total} is the total charge, and α and v are the constant and scan rate, respectively. Therefore, using eqn (3), $q_{\text{capacitive}}$ was calculated by extrapolating $q(v)$ to $v = \infty$ in the plot of $q(v)$ *vs.* $v^{-1/2}$. Furthermore, using eqn (4), q_{total} was obtained by extrapolating $q(v)$ to $v = 0$ in plots of $1/q(v)$ *vs.* $v^{1/2}$.^{21,47,48} As shown in Fig. 3g and h, the values of $q_{\text{capacitive}}$ and q_{total} were 367 mA h g⁻¹ and 467 mA h g⁻¹, respectively (*vs.* lithium ions). The total charge was in good agreement with the maximum specific capacity (447.7 mA h g⁻¹) obtained at 0.1 mV s⁻¹. The ratio of the capacitive charge to the total charge was 78.5%. Similarly, the $q_{\text{capacitive}}$ and q_{total} were 330 mA h g⁻¹ and 395 mA h g⁻¹, respectively (*vs.* sodium ions), as shown in Fig. 3i and j. The derived ratio of the capacitive charge to the total charge was 83.5%. As expected, these values were in good agreement with the results obtained using the first method (Fig. 3e and f; 76.7% and 81.5% at 0.1 mV s⁻¹ for lithium and sodium ions, respectively).

Extremely high capacitive contribution ratios were confirmed for both lithium and sodium intercalation reactions, showing that these lithium and sodium ion intercalation processes were more capacitive-dominated throughout the potential range. Furthermore, we speculated that the stored lithium or sodium ions were derived from both surface/near-surface reactions and

interior intercalation with WSe₂. As the intrinsic 2D layered structure of WSe₂ with large interlayer spacing could facilitate ion diffusion, the unique onion-like structure provided more edges for ion insertion/deinsertion. These structural factors afforded a kinetically facile intercalation process in WSe₂. Refinement of the structure after insertion/deinsertion further shortened the ion diffusion path. Furthermore, decreased charge transfer resistance alleviated the ohmic constrain of the electrode, leading to an extremely high capacitive contribution.

Meanwhile, sodium ions are expected to be stored in WSe₂ faster than lithium ions due to the higher capacitive contribution ratio. Therefore, the time dependence of the stored charge capacity was compared, as shown in Fig. 3k. Both lithium and sodium ion storage were distinctly time dependent. Notably, 48.6% of the total amount of charge could be stored for the initial 30 s, corresponding to sodium ions exhibiting an exceptionally fast charging ability. As the charging time reached at 120 s, 69.7% of the total amount of charge was delivered *vs.* sodium, while only 55.7% was obtained *vs.* lithium, demonstrating the high efficiency of sodium ion storage over lithium ion storage.

The interesting electrochemical behavior diversity, particularly the highly efficient sodium ion storage capability compared with that of lithium ions, must be associated with the insertion/deinsertion mechanism. The lithiation/delithiation mechanism was analyzed in detail by Yang *et al.*³² The reaction was as follows: WSe₂ + 4Li⁺ + 4e⁻ ↔ W + 2Li₂Se. Specifically, during the discharge process, lithium ions intercalate with WSe₂, forming Li₂Se and W, where W is embedded in the Li₂Se matrix, namely Li_xWSe₂. Subsequently, during the charging process, lithium ions are extracted from Li_xWSe₂ and WSe₂ is recovered reversibly. This reported mechanism is consistent with those of MoS₂ and MoSe₂.⁴⁹⁻⁵² We also investigated the lithiation/delithiation mechanism of WSe₂ by *ex situ* XRD and *ex situ* Raman, as shown in Fig. S6 (ESI[†]), which was also consistent with a previous report.³² However, the sodiation/desodiation mechanism remains controversial. Accordingly, *ex situ* XRD, *ex situ* Raman, and *ex situ* TEM with respect to the sodiation/desodiation process were performed. Fig. 4a and b show the *ex situ* XRD patterns of WSe₂ obtained during the initial two charge/discharge cycles in the potential range 0.01–3.0 V at a current density of 50 mA g⁻¹. Ten typical stages were selected during the charge/discharge process, as shown in Fig. 4a. All measured electrodes were protected by a preservative film in the glovebox, avoiding the effect of oxidation under ambient conditions. As shown in Fig. 4b, the XRD pattern of the open circuit voltage (OCV) state (point 1) electrode was mainly indexed to WSe₂. Characteristic peaks around 22° and 23° were attributed to the preservative film, as confirmed in Fig. S7 (ESI[†]). For the discharge process at 1.0 V (point 2), no obvious change in WSe₂ was observed. After the first potential plateau at 0.25 V (point 3), the WSe₂ characteristic peaks disappeared and new diffraction peaks at around 21° and 37° were detected and assigned to the Na₂Se phase. Another peak at around 35° might be due to the SEI layer. After the discharge process, in the charge process at 1.2 V (point 4) no obvious change was identified except for the slightly weaker Na₂Se peaks, indicating sodium ion extraction from Na₂Se. At the end of the charge

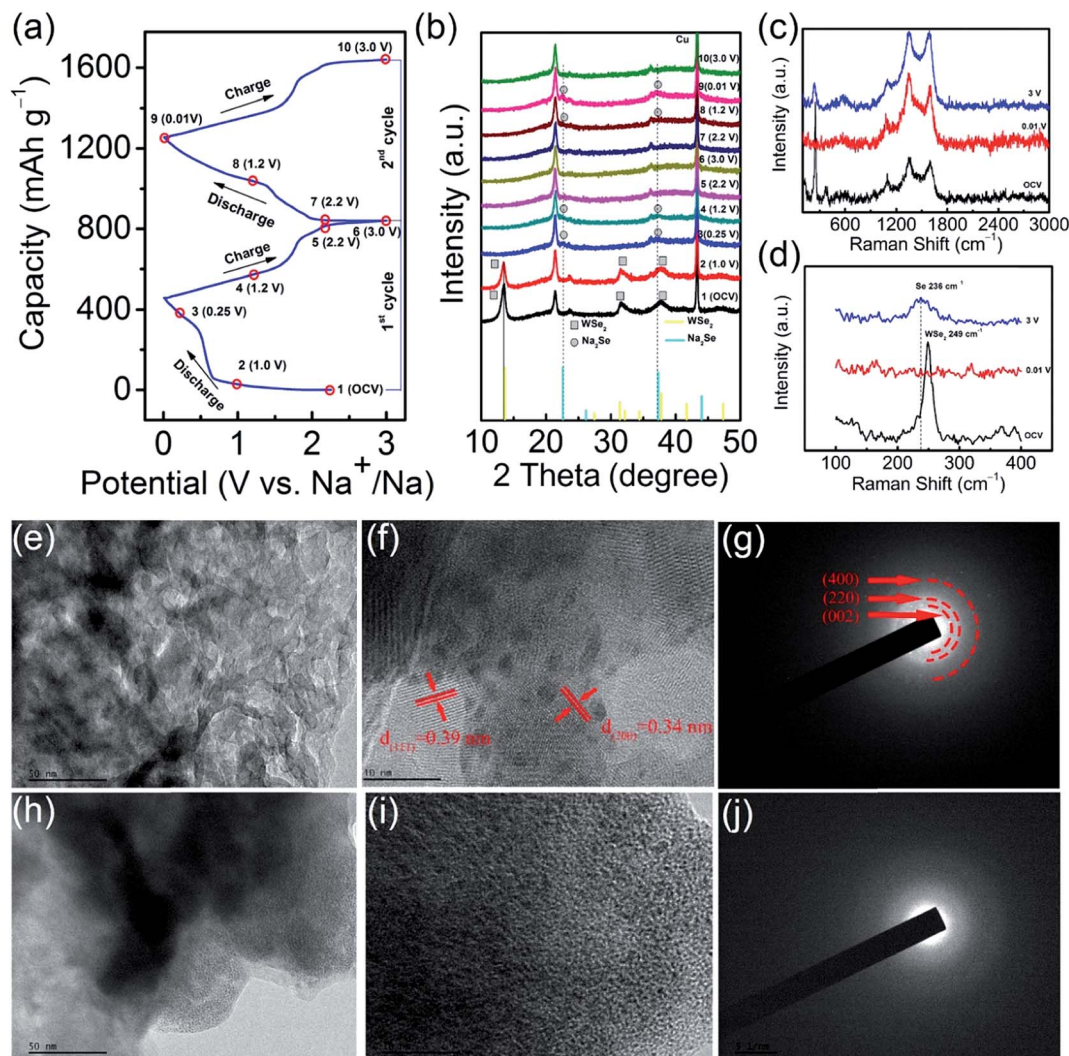
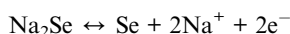
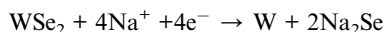


Fig. 4 Mechanism analysis of sodiation/desodiation: (a) Initial two discharge/charge curves. Numbers one to ten refer to different potential stages corresponding to *ex situ* XRD patterns, *ex situ* Raman spectra, and TEM images; (b) *ex situ* XRD patterns; (c) and (d) *ex situ* Raman spectra collected at the points one, nine, and ten; (e) TEM image, (f) high resolution TEM image, and (g) SAED pattern collected at point nine; (h) TEM image, (i) high resolution TEM image, and (j) SAED pattern collected at point ten.

processes at 2.2 and 3.0 V (points 5 and 6), the Na_2Se peaks had fully disappeared, indicating that desodiation had finished. Notably, the pristine peaks attributed to WSe_2 could not be detected, suggesting that WSe_2 with a high degree of crystallinity could not be confirmed or WSe_2 could not be recovered completely. During the subsequent discharge/charge process, the same phenomenon was obtained, namely, the Na_2Se phase was formed in the discharge process (sodiation) and disappeared during the charge process (desodiation), demonstrating good electrochemical reversibility. To further determine the sodiation/desodiation mechanism, *ex situ* Raman spectroscopy was conducted, as shown in Fig. 4c and d. A characteristic peak at 249 cm^{-1} was assigned to pristine WSe_2 in the OCV state. For the discharge state at 0.01 V (point 9), no obvious signal was detected in the Raman shift range of $100\text{--}400\text{ cm}^{-1}$, while a peak at 236 cm^{-1} indexed to the chain-structured Se molecules was identified.⁵³ This result indicated that Se was converted after the desodiation process. The inner

structure of the electrode material at different charge/discharge stages was determined by TEM, as shown in Fig. 4e–j. Compared with pristine WSe_2 , the electrode in the discharge state at 0.01 V (point 9) exhibited a more fine framework (Fig. 4e), indicating rearrangement after initial sodiation/desodiation. Very fine particles with average sizes of 3 nm and amorphous features were observed and corresponded to separated and condensed amorphous W clusters (Fig. 4f). Lattice fringes with interplanar spacings of 0.39 and 0.34 nm corresponded to the (111) and (200) planes of Na_2Se phase (Fig. 4g), respectively, which were consistent with the XRD results. The corresponding SAED pattern was obtained, as shown in the inset, which was relevant to the (002), (220), and (400) planes of Na_2Se phase, respectively. For the charge state at 3.0 V (point 10) (Fig. 4h–j), no obvious phase with a relatively high degree of crystallinity was observed, and the separated W nanoparticles maintained the initial state, indicating reversible Na_2Se desodiation and irreversible WSe_2 formation. Furthermore, the

structural evolution of the electrodes after cycling with respect to both lithium and sodium ions was observed, as shown in the SEM images (Fig. S8, ESI†). Combined with the XRD, Raman, and TEM results, a sodiation/desodiation mechanism was proposed in this study, in which the reactions proceed *via* two steps, namely, intercalation and conversion reactions, which can be expressed using the following reaction equations:



In the initial sodiation process (discharging), sodium ions intercalate with the interlayers of WSe_2 , forming WNa_xSe_2 . WNa_xSe_2 then decomposes into W and Na_2Se . During the desodiation process (charging), the conversion reaction occurs in Na_2Se . Sodium ions are extracted step-by-step, starting from Na_2Se , and converting to Na_{2-x}Se and eventually Se. The as-formed Se was kinetically stable and did not react with separated W to recover pristine WSe_2 . Next, sodium ions react with the transformed Se reversibly during the subsequent charge/discharge process. This multistep reaction is also consistent with the reported sodiation/desodiation mechanism of bare Se.⁵⁴ Reconsidering the above CV and galvanostatic charge/discharge profiles *vs.* sodium ions (Fig. 2d and e) in the 1st CV curve, the reduction peak at 0.46 V was associated with the intercalation reaction and as-decomposed Na_2Se . The oxidation peaks at 2.13 and 1.81 V were attributed to the gradual conversion of Na_2Se into Se. The conversion reactions are highly reversible, as shown starting from the 2nd CV scan. In the galvanostatic charge/discharge profiles, the potential plateau of the 1st discharge process differed from the subsequent charge/discharge, while two obvious potential plateaus were observed, proving the segmented conversion reactions of Na_2Se to Se. The proposed sodiation/desodiation mechanism was well depicted by the

electrochemical behavior, but was distinctly different to the lithiation/delithiation mechanism.³² Furthermore, the diffusion rate of lithium and sodium ions through the electrode were calculated, as shown in Fig. S9 (ESI†). The higher slope suggested a faster diffusion rate for sodium ions than for lithium ions, which might be due to conductivity enhancement from the separated metallic W in the electrode.

The sodiation/desodiation mechanism was proposed based on experimental results, but to gain further insight into the intrinsic mechanism of sodiation/desodiation, we also performed extensive structural searching starting from sodium and WSe_2 (Na_xWSe_2) using USPEX and CALYPSO codes within density functional theory. Interestingly, our structure searches uncovered two relatively stable phases of Na_2WSe_2 and $\text{Na}_{3.75}\text{WSe}_2$ (Fig. 5a), of which $\text{Na}_{3.75}\text{WSe}_2$ was the most energetically favorable on the convex hull. Furthermore, structural examination of these two phases showed that Na atoms had a strong affinity for Se atoms, such that W atoms are pushed out to form cluster-like configurations in the host material (irregular W_4 tetrahedron in $\text{Na}_{3.75}\text{WSe}_2$ and W_4 rhombohedra in Na_2WSe_2 , as shown in Fig. 5b), which was consistent with the TEM observations. This result indicated that the $\text{Na}_{3.75}\text{WSe}_2$ could be obtained at the beginning of phase transformation during the sodiation process. The calculated crystal orbital Hamilton population (COHP) curves (Fig. 5c and d) showed a large W–Se antibonding region around the Fermi level in both Na_2WSe_2 and $\text{Na}_{3.75}\text{WSe}_2$, suggesting their metastable nature, which was due to the larger separation of W atoms in the host structures. Although Na_2WSe_2 and $\text{Na}_{3.75}\text{WSe}_2$ were energetically favorable, both were inclined to decompose immediately during sodiation, which might explain the difficulty in their observation during the discharge process due to the metastable behavior of the phase. Based on this speculation, the global energy differences for every possible constituent, namely Na, W,

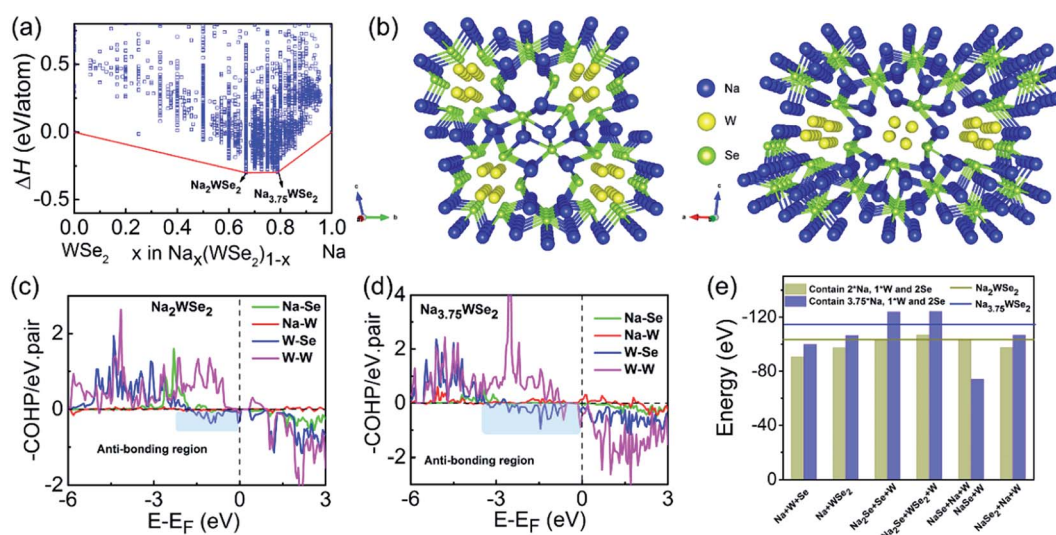


Fig. 5 (a) Calculated convex hull of $\text{Na}_x(\text{WSe}_2)_{1-x}$ for candidates obtained from structural searching, with the phases on the lines indicating its thermodynamic stability. (b) Structures of relatively stable phases of Na_2WSe_2 (left) and $\text{Na}_{3.75}\text{WSe}_2$ (right), containing irregular W_4 cluster-like configurations. Calculated crystal orbital Hamilton population (COHP), for (c) Na_2WSe_2 , (d) $\text{Na}_{3.75}\text{WSe}_2$, and (e) the global energy comparison of Na_2WSe_2 and $\text{Na}_{3.75}\text{WSe}_2$ with different constituent elements/compounds.

Se, WSe_2 , Na_2Se , NaSe , and NaSe_2 , were calculated in comparison with those of metastable Na_2WSe_2 and $\text{Na}_{3.75}\text{WSe}_2$. The energetic competitions shown in Fig. 5e suggested that the previous most stable $\text{Na}_{3.75}\text{WSe}_2$ would decompose into two potential routes, namely, $\text{Na}_2\text{Se} + \text{WSe}_2 + \text{W}$ ($-2.42 \text{ eV f.u.}^{-1}$) and $\text{Na}_2\text{Se} + \text{Se} + \text{W}$ ($-2.32 \text{ eV f.u.}^{-1}$). The presence of Na_2Se was in agreement with the obtained XRD and TEM results, in which the corresponding characteristic peaks were identified. Meanwhile, there was no signal belonging to Se detected in the Raman spectra at the end of the sodiation process, which inferred that $\text{Na}_{3.75}\text{WSe}_2$ could decompose to $\text{Na}_2\text{Se} + \text{WSe}_2 + \text{W}$ during the sodiation process. The as-decomposed WSe_2 might still intercalate with subsequent sodium ions until the end of the sodiation process. At this stage, the final products were Na_2Se and W. W atoms with low crystallinity tend to condense in the host material, which is difficult to identify by XRD. During the desodiation process, intercalated sodium ions were extracted, leaving Se and W individually, rather than recovering the pristine phase of WSe_2 , which was consistent with the identified characteristic peaks of Se in the Raman spectra at the end of the desodiation process. Our calculations agreed well with experimental observations, providing further support for the proposed sodiation/desodiation mechanism.

Furthermore, the lithiation/delithiation process was also performed using the method shown in Fig. S10.† Based on the lithiation, two relatively stable phases of $\text{Li}_{3.667}\text{WSe}_2$ and Li_6WSe_2 could be obtained (Fig. S10a†). Notably, W atoms in Li-WSe_2 were dramatically different to those in Na-WSe_2 (Fig. S10b†). W atoms in Na-WSe_2 were condensed into localized W-W chains. In contrast, W atoms in Li-WSe_2 formed a monoatomic metal layer with longer W-W separation. The calculated ICOHP (integrated crystal-orbital Hamilton population) value showed that the bonding strength of W-W pairs in $\text{Na}_{3.75}\text{WSe}_2$ was stronger than for those in Li-WSe_2 , especially in $\text{Na}_{3.75}\text{WSe}_2$ (Table S2†). Therefore, during the desodiation process, the localized metal chains and strong W-W bonding in Na-WSe_2 were considered to restrict WSe_2 recovery, whereas the WSe_2 phase could be recovered, except for the structural refinement during the delithiation process, which was in stark contrast to the abovementioned lithiation/delithiation mechanism. These results also supported the better rate capability of WSe_2 vs. sodium ions.

The proposed lithiation/delithiation and sodiation/desodiation mechanisms are shown in Fig. S11a† and 6a. Compared with the reversible conversion and structure refinement of WSe_2 based upon lithiation/delithiation, amorphous or

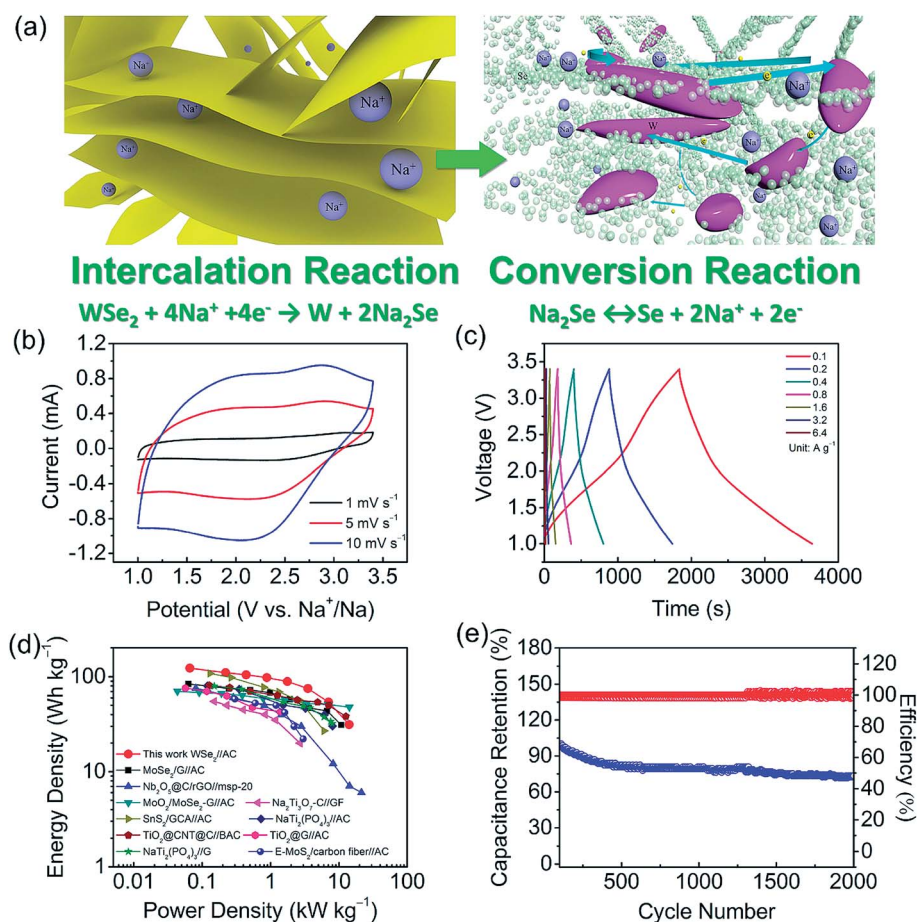


Fig. 6 (a) Schematic illustration of proposed sodiation/desodiation mechanism of WSe_2 , (b) CV curves, (c) galvanostatic charge/discharge profiles of SICs full-cell based on the WSe_2 anode and AC cathode, (d) Ragone plots, and (e) cyclic stability of SICs full cell at a current density of 1000 mA h g^{-1} .

nanostructured W was separated and condensed rather than reacted with desodiated Se to recover pristine WSe₂ after the initial sodiation/desodiation process, leading to conductivity enhancement of the electrode. As such, sodium ions make a higher capacitive contribution than lithium ions in WSe₂. Accordingly, SICs and LICs were assembled to evaluate their potential for practical applications. WSe₂ and AC were used as the anode and cathode, respectively. The cathode to anode mass ratio should be balanced and the typical performance of AC was selected based on our previous reports.^{55,56} SICs with a 3 : 1 ratio exhibited an optimized performance (Fig. 6b–e) (electrochemical performances of LICs are shown in Fig. S11b–e, ESI†), which strongly depended on the measured potential window. Therefore, the CV curves at various potential windows were measured, as shown in Fig. S12a.† A suitable potential window of 1.0–3.4 V was determined, otherwise a minor distorted CV shape would deteriorated the SIC performance due to possible side reactions between electrode and electrolyte. The typical CV curves at various scan rates and the corresponding galvanostatic charge/discharge profiles at various current densities in the potential range of 1.0–3.4 V are shown in Fig. 6b and c, respectively. The plots exhibit a segmented feature with different slopes (Fig. 6c), demonstrating the integrated mechanisms of EDLCs and batteries. The maximum specific capacitance (81 F g⁻¹) of as-assembled SICs was obtained at a current density of 30 mA g⁻¹ (Fig. S12b†). The SICs exhibit superior energy/power densities, as shown in the Ragone plots (Fig. 6d). Specifically, the maximum energy density of 123.1 W h kg⁻¹ at the power density of 66.0 W kg⁻¹ was achieved, and the energy density decreased slightly with increasing power density. When the powder density was increased to 7.0 and 14.1 kW kg⁻¹, energy densities of 54.0 and 31.3 W h kg⁻¹ were maintained. These results outperformed several previous reports in the Ragone Plots (Fig. 6d), such as MoSe₂/G//AC,⁵⁷ Nb₂O₅@C/rGO//msp-20,⁵⁸ MoO₂/MoSe₂-G//AC,⁵⁹ SnS₂/GCA//AC,⁶⁰ TiO₂@CNT@C//BAC,⁶¹ NaTi₂(PO₄)₃/G,⁶² Na₂Ti₃O₇-C//GF,⁶³ NaTi₂(PO₄)₃//AC,⁶⁴ TiO₂@G//AC,⁶⁵ and E-MoS₂/carbon fiber//AC,⁶⁶ demonstrating the great potential as the anode for SICs. Furthermore, the LICs could deliver a maximum energy density of 80.1 W h kg⁻¹ at a power density of 66.0 W kg⁻¹ and a maximum power density of 14.1 kW kg⁻¹ at an energy density of 2.7 W h kg⁻¹. This inferior performance compared with the SICs was attributed to the dramatically different intercalation mechanism, demonstrating that WSe₂-based SICs could deliver a superior energy/power output over LICs. Fig. 6e exhibits the cycling stability of the SICs, demonstrating a capacitance retention of 75% after 2000 cycles at a current density of 1000 mA g⁻¹ with a nearly 100% coulombic efficiency, whereas the LICs delivered a 91.5% capacitance retention after 10 000 cycles (Fig. S11e, ESI†). The degraded cyclic stability of SICs can be ascribed to the significant structure change derived from the sodiation/desodiation process and larger ionic radius of sodium ion. Considering the high theoretical density of WSe₂ (9.32 g cm⁻³), the WSe₂ anode also has promising applications in SICs with high volumetric performances. According to the systematic characterizations, the WSe₂ anode for SICs exhibits superior performance that could rival LICs, providing new

insight into novel 2D TMD design for SICs with the high energy and power densities.

3. Conclusions

In summary, onion-like WSe₂ nanoparticles were synthesized using a homemade CVD method. The very fine particle size and unique microstructure were attributed to the fast cooling rate and reduction in surface energy of 2D WSe₂ after nucleation and growth. Superior electrochemical performances were obtained under the evaluation of both lithium and sodium ion chemistries. An exceptionally high ratio of capacitive contribution that ensured fast intercalation kinetics was identified, which was attributed to the intrinsic properties and the unique microstructure of WSe₂. Sodium ions were stored faster throughout WSe₂ than lithium ions, which was due to the different intercalation mechanisms that were concluded by electrochemical investigation and simulation. The SICs delivered superior energy/power densities, demonstrating WSe₂ as a promising alternative for SICs that could rival LICs and shedding new light on novel 2D TMD design for SICs with high energy and power densities.

4. Experimental section

Synthesis of WSe₂ nanoparticles

W(CO)₆ and pure selenium were used as W and Se precursors, respectively. The carrier gas (high purity argon) was passed through a heated bubbling unit containing W(CO)₆ at an evaporation temperature of 120 °C. The homemade dual-temperature zone reactor is shown in Fig. S1.† The quartz boat containing pure Se powder was placed in the low-temperature zone in advance. The low-temperature zone was maintained at a temperature of 430 °C to evaporate Se. The mixed gas containing W and Se precursors passed through the high-temperature zone, where W reacted with Se in the gas phase at 950 °C. The resultant product was deposited and collected in the water-cooled chamber. Se was always in excess throughout the experiment. To remove excess Se, the as-prepared powder was heat-treated in a hydrogen gas flow at a temperature of 570 °C to obtain the final WSe₂ nanoparticles. Commercial WSe₂ (Aladdin Ltd.) was purchased as the control sample.

Characterizations

Powder XRD (Bruker D8-focus X-ray powder diffractometer) with Cu K α radiation ($\lambda = 1.5406 \text{ \AA}$) was used to analyze the crystalline phase of the material in the 2θ range of 8° to 80° at room temperature. The sample morphology and microstructure were observed using field emission scanning electron microscopy (FESEM, JEOL JSM-7100F) and transmission electron microscopy (TEM, Tecnai LaB6). The crystalline structure of the as-prepared sample was determined using high-resolution TEM (HRTEM). The chemical or electronic state of the elements was measured at room temperature using X-ray photoelectron spectroscopy (XPS, Thermo Scientific ESCALAB 250XI Probe system). Raman spectra were measured using a spectrometer

(inVia Reflex, Renishaw, UK) with a laser excitation wavelength of 532 nm in the range of 100–500 cm^{-1} .

Electrochemical measurements

All types of half cells and full cells were assembled using coin cells (CR2032) in an argon-filled glove box. The as-synthesized WSe_2 nanoparticles (75 wt%), super P (15 wt%), and binder (10 wt%) (carboxymethyl cellulose (CMC)) were mixed and dissolved in DI water to form a slurry, which was uniformly coated on copper foil and dried at 60 °C for 12 h to afford the anode. The mass density of the active material in each electrode was 1.2–1.8 mg cm^{-2} . The cathode was fabricated by mixing commercial activated carbon (AC) (80 wt%), super P (10 wt%), and polyvinylidene fluoride (PVDF, 10 wt%) binder in *N*-methyl-2-pyrrolidone (NMP) and coating uniformly on carbon-coated Al foil. For lithium ion half cells, lithium foil, polypropylene film (Celgard 2400), and a solution of 1.0 M LiPF_6 in ethylene carbonate/diethyl carbonate (1 : 1 : 1, v/v/v) were used as the counter and reference electrodes, separator, and electrolyte, respectively. Glass fiber and a solution of 1.0 M NaClO_4 in ethylene carbonate/diethyl carbonate (1 : 1, v/v) with 5 vol% fluoroethylene carbonates were selected as separator and electrolyte for the sodium ion half cells. Sodium foil was used as both the counter and reference electrode. For LIC and SIC full-cell measurements, the as-prepared AC electrode was used as cathode. The WSe_2 anode was pretreated after two cycles at a current density of 100 mA g^{-1} in each half cell. The pre-discharged WSe_2 anodes were disassembled and reassembled with AC cathode into the LIC and SIC full cells in an Ar-filled glove box. Commercial WSe_2 was used in the same test procedure. Cyclic voltammetry (CV) was performed at various scan rates in a potential range of 0.01–3 V using an electrochemical workstation (Ametek, Princeton Applied Research, Versa STAT 4). Electrochemical impedance spectroscopy (EIS) was conducted in the frequency range of 100 KHz to 0.01 Hz. Galvanostatic charge/discharge measurements were performed at different current rates (0.1–0.8 A g^{-1}) using a multichannel battery testing system (Neware BTS4000) in the potential range of 0.01–3.0 V. All potentials were vs. Li^+/Li for lithium ions and Na^+/Na for sodium ions. The cutoff potentials were set as 3.0–4.5 V, 1.0–3.4 V vs. Li^+/Li , and 1.0–3.4 V for the AC cathode, LIC full cells, and SIC full cells, respectively. All electrochemical measurements were performed at room temperature. The following formula, $C_s (\text{F g}^{-1}) = \frac{I \times \Delta t}{3600 \times m} = C (\text{mA h g}^{-1}) \times \frac{3600}{dV}$, was used to convert the specific capacity into specific capacitance, where I (A) is the constant current, Δt (s) is the discharge time, m (g) is the mass of active materials, C (mA h g^{-1}) is the specific capacity, and dV (mV) is the potential window. The energy density (E , Wh kg^{-1}) and power density (P , W kg^{-1}) of the LIC and SIC full cells were calculated using the following equations: $E = \int_{t_1}^{t_2} IV dt = \frac{1}{2} C (V_{\text{max}} + V_{\text{min}}) (V_{\text{max}} - V_{\text{min}}) = \Delta V \times \frac{I}{m} \times t$, $P = \frac{E}{t} = \Delta V \times \frac{I}{m}$, $\Delta V = \frac{V_{\text{max}} + V_{\text{min}}}{2}$, where V_{max} and V_{min} are the initial and final discharge potentials (V) and m is the total mass of active materials in the anode and cathode.

Ab initio calculations

USPEX and CALYPSO codes were used to search for low-enthalpy structures with compositions of Na_xWSe_2 and Li_xWSe_2 .^{67,68} Structure relaxations were conducted using density functional theory (DFT) within the generalized gradient approximation (GGA) of Perdew–Burke–Ernzerhof (PBE) as implemented in the VASP code.^{69,70} The all-electron projector augmented wave scheme (PAW) was adopted with valence electrons of Na ($2p^6 3s^1$), W ($6s^2 5d^4$) and Se ($4s^2 4p^4$).^{71,72} A plane-wave kinetic energy cutoff energy of 600 eV and Brillouin zone sampling grid with a resolution of $2\pi \times 0.03 \text{ \AA}^{-1}$ was tested to ensure the enthalpy calculations converged well within 1 meV per atom. Crystal-orbital Hamilton population (COHP) analyses were calculated using the LOBSTER program.^{73–75}

Conflicts of interest

The authors declare no conflicts of interest.

Acknowledgements

Y. C. W. and X. Z. contributed equally to this work. We acknowledge financial support from the National Natural Science Foundation of China (No. 51502073), Natural Science Foundation of Tianjin, China (No. 15JCYBJC53200), Natural Science Foundation of Hebei Province, China (No. E2018202123), and Key Research and Development Program of Hebei Province, China (No. 17391001D).

References

- M. R. Lukatskaya, B. Dunn and Y. Gogotsi, *Nat. Commun.*, 2016, **7**, 12647.
- S. Chu and A. Majumdar, *Nature*, 2012, **488**, 294.
- P. Simon, Y. Gogotsi and B. Dunn, *Science*, 2014, **343**, 1210–1211.
- P. Simon and Y. Gogotsi, *Nat. Mater.*, 2008, **7**, 845–854.
- W. Huanwen, Z. Changrong, C. Dongliang, Y. Qingyu and F. H. Jin, *Adv. Mater.*, 2017, **29**, 1702093.
- L. Bing, Z. Junsheng, Z. Hongyou, J. Liming, Y. Daijun, L. Hong, S. Chao, S. Annadanesh, Z. Yiran, G. Ruiqi, J. P. Zheng and Z. Cunman, *Adv. Mater.*, 2018, **30**, 1705670.
- Z. Lin, E. Goikolea, A. Balducci, K. Naoi, P. L. Taberna, M. Salanne, G. Yushin and P. Simon, *Mater. Today*, 2018, **21**(4), 419–436.
- V. Aravindan, J. Gnanaraj, Y.-S. Lee and S. Madhavi, *Chem. Rev.*, 2014, **114**, 11619–11635.
- K. Naoi, S. Ishimoto, J.-i. Miyamoto and W. Naoi, *Energy Environ. Sci.*, 2012, **5**, 9363–9373.
- L. Shen, H. Lv, S. Chen, P. Kopold, A. van Aken Peter, X. Wu, J. Maier and Y. Yu, *Adv. Mater.*, 2017, **29**, 1700142.
- X. Qiuying, Y. Hai, W. Min, Y. Mei, G. Qiubo, W. Liming, X. Hui and Y. Yan, *Adv. Energy Mater.*, 2017, **7**, 1701336.
- M. Yanfeng, C. Huicong, Z. Miao and C. Yongsheng, *Adv. Mater.*, 2015, **27**, 5296–5308.

- 13 X. Zhao, H. E. Wang, J. Cao, W. Cai and J. Sui, *Chem. Commun.*, 2017, **53**, 10723–10726.
- 14 Y. Tang, Y. Zhang, W. Li, B. Ma and X. Chen, *Chem. Soc. Rev.*, 2015, **44**, 5926–5940.
- 15 Y. Lu, L. Yu and X. W. Lou, *Chem*, 2018, **4**, 972–996.
- 16 Z. Limin, Z. Kai, H. Zhe, T. Zhanliang, M. Liqiang, K. Yong-Mook, C. Shu-Lei and C. Jun, *Adv. Energy Mater.*, 2018, **8**, 1701415.
- 17 H.-E. Wang, X. Zhao, X. Li, Z. Wang, C. Liu, Z. Lu, W. Zhang and G. Cao, *J. Mater. Chem. A*, 2017, **5**, 25056–25063.
- 18 Y. Cai, H. E. Wang, X. Zhao, F. Huang, C. Wang, Z. Deng, Y. Li, G. Cao and B. L. Su, *ACS Appl. Mater. Interfaces*, 2017, **9**, 10652–10663.
- 19 T. Brezesinski, J. Wang, S. H. Tolbert and B. Dunn, *Nat. Mater.*, 2010, **9**, 146–151.
- 20 V. Augustyn, J. Come, M. A. Lowe, J. W. Kim, P. L. Taberna, S. H. Tolbert, H. D. Abruña, P. Simon and B. Dunn, *Nat. Mater.*, 2013, **12**, 518–522.
- 21 J. B. Cook, K. Hyung-Seok, Y. Yan, J. S. Ko, R. Shauna, D. Bruce and S. H. Tolbert, *Adv. Energy Mater.*, 2016, **6**, 1501937.
- 22 Y. Gogotsi and R. M. Penner, *ACS Nano*, 2018, **12**, 2081–2083.
- 23 Q. Wei, Q. Wang, Q. Li, Q. An, Y. Zhao, Z. Peng, Y. Jiang, S. Tan, M. Yan and L. Mai, *Nano Energy*, 2018, **47**, 294–300.
- 24 Z. Teng, S. Shuo, L. Xiaojing, L. Chaolun, W. Gongming and X. Hui, *Adv. Mater.*, 2018, **30**, 1706640.
- 25 L. Baosong, X. Baojuan, F. Zhenyu, L. Yue, L. Jincheng, F. Jinkui, Q. Yitai and X. Shenglin, *Adv. Mater.*, 2018, **30**, 1705788.
- 26 X. Wang and G. Shen, *Nano Energy*, 2015, **15**, 104–115.
- 27 Z. Yue, P. Lele, F. Zhiwei, Y. Chunshuang, Z. Xiao and Y. Guihua, *Adv. Mater.*, 2018, **30**, 1706347.
- 28 X. Zhao, J. Sui, F. Li, H. Fang, H. Wang, J. Li, W. Cai and G. Cao, *Nanoscale*, 2016, **8**, 17902–17910.
- 29 W. Hua, F. Hongbin and L. Jinghong, *Small*, 2014, **10**, 2165–2181.
- 30 Y. Y. Lee, G. O. Park, Y. S. Choi, J. K. Shon, J. Yoon, K. H. Kim, W.-S. Yoon, H. Kim and J. M. Kim, *RSC Adv.*, 2016, **6**, 14253–14260.
- 31 J. Wang, L. Chen, L. Zeng, Q. Wei and M. Wei, *ACS Sustainable Chem. Eng.*, 2018, **6**, 4688–4694.
- 32 W. Yang, J. Wang, C. Si, Z. Peng and Z. Zhang, *Nano Res.*, 2017, **10**, 2584–2598.
- 33 F. Chen, J. Wang, B. Li, C. Yao, H. Bao and Y. Shi, *Mater. Lett.*, 2014, **136**, 191–194.
- 34 A. Eftekhari, *J. Mater. Chem. A*, 2017, **5**, 18299–18325.
- 35 K. Share, J. Lewis, L. Oakes, R. E. Carter, A. P. Cohn and C. L. Pint, *RSC Adv.*, 2015, **5**, 101262–101267.
- 36 J. Zhou, J. Qin, L. Guo, N. Zhao, C. Shi, E.-z. Liu, F. He, L. Ma, J. Li and C. He, *J. Mater. Chem. A*, 2016, **4**, 17370–17380.
- 37 Z. Zhang, X. Yang and Y. Fu, *RSC Adv.*, 2016, **6**, 12726–12729.
- 38 X. Zhao, H. E. Wang, R. C. Massé, J. Cao, J. Sui, J. Li, W. Cai and G. Cao, *J. Mater. Chem. A*, 2017, **5**, 7394–7402.
- 39 W. Li, D. Chen, F. Xia, J. Z. Y. Tan, J. Song, W.-G. Song and R. A. Caruso, *Chem. Commun.*, 2016, **52**, 4481–4484.
- 40 P. Tonndorf, R. Schmidt, P. Böttger, X. Zhang, J. Börner, A. Liebig, M. Albrecht, C. Kloc, O. Gordan, D. R. T. Zahn, S. Michaelis de Vasconcellos and R. Bratschitsch, *Opt. Express*, 2013, **21**, 4908–4916.
- 41 L. Hai, L. Gang, W. Yanlong, Y. Zongyou, C. Chunxiao, H. Qiyuan, W. Lu, D. Feng, Y. Ting and Z. Hua, *Small*, 2013, **9**, 1974–1981.
- 42 H. Wang, D. Kong, P. Johanes, J. J. Cha, G. Zheng, K. Yan, N. Liu and Y. Cui, *Nano Lett.*, 2013, **13**, 3426–3433.
- 43 N. D. Boscher, C. J. Carmalt and I. P. Parkin, *J. Mater. Chem.*, 2006, **16**, 122–127.
- 44 W. Gongkai, S. Xiang, L. Fengyuan, S. Hongtao, Y. Mingpeng, J. Weilin, L. Changsheng and L. Jie, *Small*, 2012, **8**, 452–459.
- 45 J. Wang, J. Polleux, J. Lim and B. Dunn, *J. Phys. Chem. C*, 2007, **111**, 14925–14931.
- 46 M. Sathiy, A. S. Prakash, K. Ramesha, J. M. Tarascon and A. K. Shukla, *J. Am. Chem. Soc.*, 2011, **133**, 16291–16299.
- 47 S. Ardizzone, G. Fregonara and S. Trasatti, *Electrochim. Acta*, 1990, **35**, 263–267.
- 48 K. M. Lin, K. H. Chang, C. C. Hu and Y. Y. Li, *Electrochim. Acta*, 2009, **54**, 4574–4581.
- 49 K. Chang and W. Chen, *Chem. Commun.*, 2011, **47**, 4252–4254.
- 50 C. Kun, G. Dongsheng, L. Xifei, Y. Jinli, T. Yongji, C. Mei, L. Ruying and S. Xueliang, *Adv. Energy Mater.*, 2013, **3**, 839–844.
- 51 Q. Wang and J. Li, *J. Phys. Chem. C*, 2007, **111**, 1675–1682.
- 52 J. Yao, B. Liu, S. Ozden, J. Wu, S. Yang, M.-T. F. Rodrigues, K. Kalaga, P. Dong, P. Xiao, Y. Zhang, R. Vajtai and P. M. Ajayan, *Electrochim. Acta*, 2015, **176**, 103–111.
- 53 C. Luo, Y. Xu, Y. Zhu, Y. Liu, S. Zheng, Y. Liu, A. Langrock and C. Wang, *ACS Nano*, 2013, **7**, 8003–8010.
- 54 Q. Li, H. Liu, Z. Yao, J. Cheng, T. Li, Y. Li, C. Wolverton, J. Wu and V. P. Dravid, *ACS Nano*, 2016, **10**, 8788–8795.
- 55 G. Wang, C. Lu, X. Zhang, B. Wan, H. Liu, M. Xia, H. Gou, G. Xin, J. Lian and Y. Zhang, *Nano Energy*, 2017, **36**, 46–57.
- 56 X. Zhang, C. Lu, H. Peng, X. Wang, Y. Zhang, Z. Wang, Y. Zhong and G. Wang, *Electrochim. Acta*, 2017, **246**, 1237–1247.
- 57 X. Zhao, W. Cai, Y. Yang, X. Song, Z. Neale, H. E. Wang, J. Sui and G. Cao, *Nano Energy*, 2018, **47**, 224–234.
- 58 E. Lim, C. Jo, M. S. Kim, M.-H. Kim, J. Chun, H. Kim, J. Park, K. C. Roh, K. Kang, S. Yoon and J. Lee, *Adv. Funct. Mater.*, 2016, **26**, 3711–3719.
- 59 X. Zhao, H. E. Wang, Y. Yang, Z. G. Neale, R. C. Massé, J. Cao, W. Cai, J. Sui and G. Cao, *Energy Storage Mater.*, 2018, **12**, 241–251.
- 60 J. Cui, S. Yao, Z. Lu, J. Q. Huang, W. G. Chong, F. Ciucci and J. K. Kim, *Adv. Energy Mater.*, 2018, **8**, 1702488.
- 61 Y. E. Zhu, L. Yang, J. Sheng, Y. Chen, H. Gu, J. Wei and Z. Zhou, *Adv. Energy Mater.*, 2017, **7**, 1701222.
- 62 R. Thangavel, B. Moorthy, D. K. Kim and Y.-S. Lee, *Adv. Energy Mater.*, 2017, **7**, 1602654.
- 63 S. Dong, L. Shen, H. Li, G. Pang, H. Dou and X. Zhang, *Adv. Funct. Mater.*, 2016, **26**, 3703–3710.
- 64 R. Thangavel, K. Kaliyappan, K. Kang, X. Sun and Y.-S. Lee, *Adv. Energy Mater.*, 2016, **6**, 1502199.

- 65 Z. Le, F. Liu, P. Nie, X. Li, X. Liu, Z. Bian, G. Chen, H. B. Wu and Y. Lu, *ACS Nano*, 2017, **11**, 2952–2960.
- 66 C. Zhao, C. Yu, M. Zhang, Q. Sun, S. Li, M. Norouzi Banis, X. Han, Q. Dong, J. Yang, G. Wang, X. Sun and J. Qiu, *Nano Energy*, 2017, **41**, 66–74.
- 67 A. R. Oganov and C. W. Glass, *J. Chem. Phys.*, 2006, **124**, 244704.
- 68 Y. Wang, J. Lv, L. Zhu and Y. Ma, *Phys. Rev. B: Condens. Matter Mater. Phys.*, 2010, **82**, 094116.
- 69 J. P. Perdew, K. Burke and M. Ernzerhof, *Phys. Rev. Lett.*, 1996, **77**, 3865–3868.
- 70 G. Kresse and J. Furthmüller, *Comput. Mater. Sci.*, 1996, **6**, 15–50.
- 71 G. Kresse and D. Joubert, *Phys. Rev. B: Condens. Matter Mater. Phys.*, 1999, **59**, 1758–1775.
- 72 P. E. Blöchl, *Phys. Rev. B: Condens. Matter Mater. Phys.*, 1994, **50**, 17953–17979.
- 73 V. L. Deringer, A. L. Tchougréeff and R. Dronskowski, *J. Phys. Chem. A*, 2011, **115**, 5461–5466.
- 74 R. Dronskowski and P. E. Bloechl, *J. Phys. Chem.*, 1993, **97**, 8617–8624.
- 75 S. Maintz, V. L. Deringer, A. L. Tchougréeff and R. Dronskowski, *J. Comput. Chem.*, 2016, **37**, 1030–1035.